PAPER

Check for updates

Modulating Mn-doped NiO nanoparticles: structural, optical, and electrical property tailoring for enhanced hole transport layers

Robiul Islam,[†][ab] Rahim Abdur, [iD][†][b] Md. Ashraful Alam,[a] Nadim Munna, [iD][c] Aninda Nafis Ahmed,[d] Mosharof Hossain, [iD][b] Mohammad Shahriar Bashar,[b] Dipa Islam[e] and Mohammad Shah Jamal [iD] *[b]

Mn-doped NiO nanoparticles (NPs), denoted as $Ni_{1-x}Mn_xO$ with x values of 0.00, 0.02, 0.04, 0.06, and 0.08, were synthesized using a chemical precipitation process. These NPs were comprehensively analyzed for their structural, optical, and electrical properties, along with their surface morphology and elemental composition. X-ray Diffraction (XRD) confirmed the single-phase cubic crystal structure and revealed a reduction in crystallite size from 15.26 nm to 10.38 nm as Mn doping increased. Field Emission Scanning Electron microscopy (FE-SEM) determined the average particle sizes ranging from 26.03 nm to 23.30 nm. The optical properties, assessed by UV-visible spectroscopy (UV-vis), revealed a widening of the bandgap from 3.49 eV to 4.10 eV with increasing Mn doping, suggesting tunable optical characteristics. X-ray Photoelectron Spectroscopy (XPS) confirmed the presence of nickel (Ni), oxygen (O), and manganese (Mn) within the NPs. The highest mobility, $1.31 \pm 0.03 \times 10^3$ cm^2 V^{-1} s^{-1}, was observed in the 6 wt% Mn-doped NiO NPs thin film, as determined by Hall measurements. To assess their practical utility, SCAPS-1D simulation was employed, demonstrating the potential of Mn-doped NiO NPs as a hole transport layer (HTL) in perovskite solar cells (PSCs). The enhanced electrical and optical properties, combined with structural tunability, highlight Mn-doped NiO as a promising material for advanced optoelectronic applications. This study provides valuable insights into the development of efficient and stable solar cells, offering a pathway to optimize material design for improved performance in photovoltaic applications.

Introduction

The distinctive features of metal oxide nanoparticles (MONPs) make them very relevant in electrical and optoelectronic applications. MONPs are indispensable to nanoscience and nanotechnology due to their diverse characteristics, including ferroelectric, supercapacitive, superconducting, and semiconducting properties.[1] Reducing the size of MONPs accentuates their surface characteristics, allowing for tailored electrical and optical properties that are ideal for next-generation devices.[2] The solution-phase synthesis of oxide nanomaterials allows for fine control over their structure and behavior, opening the door for revolutionary applications in fields such as energy conversion and storage.[3] Nanomaterials, particularly metal oxides, have garnered immense interest due to their superior mechanical, electrical, magnetic, thermal, catalytic, and optical properties compared to their bulk counterparts.[4,5] Due to their large surface area, special adsorption properties, surface imperfections, and rapid diffusion, nano-sized crystalline metal oxides have attracted the curiosity of researchers in recent years.[6,7]

Depending on the particle size, shape, and synthesis process, nickel oxide (NiO) nanoparticles (NPs) are highly promising for various electronic and optoelectronic applications due to their wide bandgap and p-type semiconducting properties. In its nanoparticle form, NiO demonstrates enhanced semiconducting behavior, whereas bulk NiO is typically an insulator.[8] This transition from an insulating state to a semiconducting one highlights the importance of tuning

[a]Department of Applied Chemistry and Chemical Engineering, Noakhali Science and Technology University, Noakhali 3814, Bangladesh

[b]Institute of Energy Research and Development (IERD), Bangladesh Council of Scientific and Industrial Research (BCSIR), Dr Qudrat-E-Khuda Road, Dhanmondi, Dhaka 1205, Bangladesh. E-mail: msjdubd@gmail.com; msjamal@bcsir.gov.bd

[c]Institute of Mining, Mineralogy and Metallurgy (IMMM), Bangladesh Council of Scientific and Industrial Research (BCSIR), Science Laboratory Road, Khanjanpur, Joypurhat 5900, Bangladesh

[d]Pilot Plant and Process Development Centre (PP&DC), Bangladesh Council of Scientific and Industrial Research (BCSIR), Dr Qudrat-E-Khuda Road, Dhanmondi, Dhaka 1205, Bangladesh

[e]Biomedical and Toxicology Research Institute (BTRI), Bangladesh Council of Scientific and Industrial Research (BCSIR), Dr Qudrat-E-Khuda Road, Dhanmondi, Dhaka 1205, Bangladesh

† Authors contributed equally.

nanoparticle synthesis to achieve desired functionalities. The characteristics of NiO can be improved by using the right metal dopant that can give an adequate boost to the optical, electrical, and physical properties of NiO.[9] Several research groups have attempted to improve the main features of NiO by adding dopants such as copper (Cu),[10] iron (Fe),[11] cobalt (Co),[9] manganese (Mn),[12] lithium (Li),[13] and aluminum (Al).[14] Doping NiO with transition metals such as manganese (Mn) has been shown to dramatically improve its electrical, optical, and structural properties. Mn is a particularly effective dopant due to its similar ionic radius to Ni [Mn^{4+} (0.53 Å) and Ni^{2+} (0.69 Å)], allowing for easy substitution into the NiO lattice, resulting in significant enhancements in performance metrics. As a result, incorporating Mn into the NiO lattice may easily replace Ni sites while improving its structural, electrical, and optical characteristics.[15] There are several methods to synthesize Mn-doped NiO NPs, such as sol–gel,[16] wet chemical,[17] homogeneous precipitation,[18] pyrolysis,[19] and hydrothermal methods.[20,21] While each of these techniques has its merits, they are often constrained by complexity, high energy demands, and limited scalability. For instance, the sol–gel process, although capable of producing well-controlled particle sizes, typically requires complex setups and long processing times, which hinder its applicability for large-scale production. Similarly, hydrothermal methods, known for producing high-purity nanoparticles, involve high-pressure systems and prolonged heating cycles, making them impractical for cost-effective manufacturing. In contrast, the chemical precipitation method presents a significant advancement by offering simplicity and scalability, without sacrificing the quality of the nanoparticles produced.

Moreover, the hydrothermal method is one of the simplest techniques to synthesize Mn-doped NiO NPs providing homogeneous mixing, better crystallinity, uniform particle size dissemination, and smaller particle size with high purity. As a member of the metal oxide family, NiO is a p-type material with a wide bandgap and has extraordinary structural, and optical properties, with excellent chemical stability.[22,23] The amazing unique properties of NiO have made this compound a promising candidate for photovoltaic applications,[24–26] gas sensors,[27] UV photodetectors,[28] and electrochromic devices.[29] Recently scientists have been looking at NiO NPs a lot to make perovskite solar cells (PSCs) work better and last longer. People have tried putting these NPs into PSCs as a hole-transporting material (HTM) to help move charges, improve contact between layers, line up energy levels, and cut down on energy loss and recombination.[30–32] Strategies such as pre-doping NiO films with silver (Ag) ions to form a p/p^+ homojunction have shown significant improvements in charge separation, energy level alignment, and overall efficiency of PSCs.[33] NiO is tough, moves holes well, and doesn't cost much, so it could be great for the hole transport layer (HTL) in PSCs. But making it and treating it after still cause some headaches.[34] Overall, the incorporation of Mn-doped NiO nanoparticles into PSCs presents a promising strategy for significantly enhancing device performance. The tailored structural, optical, and electrical properties of these doped nanoparticles improve hole transport efficiency, which could lead to better stability and higher power conversion efficiencies. This advancement not only holds potential for improving the commercial viability of PSCs but also paves the way for broader market adoption.

In this study, we have synthesized undoped NiO and Mn-doped NiO NPs by a simple chemical precipitation process. The concentrations of Mn-dopant solution were varied in a wide range of 0, 2, 4, 6, and 8 weight percent (wt%) of NiO precursor solution. This wide range of doping concentrations were carefully controlled, allowing fine-tuning of the structural, optical, and electrical properties of the NiO NPs. Such precision in doping control is critical for optimizing the performance of these materials in different device applications. The prepared samples' structural, morphological, optical, elemental composition and valence state and electrical characteristics have been investigated to understand the Mn doping effect on NiO NPs. Also, the optical and electrical properties obtained from the investigation was used in SCAPS-1D simulation to simulate NiO NPs based thin film HTL layer in PSCs. In this case an inverted structure of PSCs with Glass\ITO\NiO\MAPbI$_3$\PCBM\Al layers.

The key innovation in this work lies in the method's ability to overcome the traditional challenges associated with NiO synthesis. By employing a straightforward chemical precipitation process, we have employed a technique that is not only more sustainable and scalable but also produces nanoparticles with enhanced functional properties tailored for advanced applications. In particular, Mn-doped NiO nanoparticles synthesized by this method exhibit superior hole transport properties, making them highly effective as a hole-transporting material (HTM) in PSCs. This improvement is critical because it leads to enhanced charge mobility, better energy alignment, and a reduction in energy loss and recombination, all of which contribute to significantly higher power conversion efficiencies (PCE) and improved stability of PSC devices. Previous research has demonstrated the potential of NiO NPs in enhancing the performance of PSCs, particularly as an HTM to facilitate charge transport and improve interfacial contact between active layers. Our Mn-doped NiO nanoparticles, synthesized via this low-temperature method, offer an even greater advantage by further improving the hole transport efficiency and tuning the electronic properties of the NiO layer. This results in better energy level alignment and more effective charge separation, leading to overall improved device performance. Additionally, the chemical stability, low cost, and ease of production of these doped NiO nanoparticles make them a highly attractive option for the commercial viability of PSCs.

Materials and methods

Materials

All compounds and solvents were used as received without further purification. Sigma-Aldrich Co. provided the following: nickel acetate dihydrate (Ni(CH$_3$COO)$_2$·2H$_2$O) (≥98%), sodium hydroxide (NaOH) (≥98%), and manganese(II) acetate tetrahydrate (Mn(CH$_3$COO)$_2$·4H$_2$O), (≥98%). The filtering procedure employed Whatman qualitative filter paper (110 mm $\varnothing$ × 100 circles).

Synthesis method of Mn-doped NiO

$Ni_{1-x}Mn_xO$ (x = 0.00, 0.02, 0.04, 0.06, and 0.08) NPs were synthesized *via* chemical precipitation process using 50 mM $(Ni(CH_3COO)_2 \cdot 4H_2O)$ and $(Mn(CH_3COO)_2 \cdot 4H_2O)$ in deionized water. 100 mM NaOH was also prepared in deionized water. Nickel acetate and manganese acetate were taken in appropriate stoichiometric ratios and mixed in separatrix glass beakers. All the solutions were heated at 80 °C and stirred on a magnetic stirrer with a hot plate for about 1 h and then deliberately chilled down to room temperature in air. Then NaOH solution was added dropwise to the solution until complete precipitation of $Ni_{1-x}Mn_x(OH)_2$. To ensure uniformity of the NPs, 6–8 drops of NaOH were added per minute to the solution with continuous stirring at 400 rpm. To ensure complete precipitation, after adding double the volume of NaOH to the solution, the mixture was allowed to settle for a while. A few additional drops of NaOH were then added to check if further precipitation occurred. Then the precipitate was filtered using Whatman filter paper and rinsed five times with DI water to remove excess NaOH. Then ppt were dried in an oven at 70 °C temperature for 24 h. After drying, the precipitates were ground into fine powders using a pulverisetter 23 (FRITSCH, Germany) at 50 Hz for 4 min with 10 balls (total weight of 2.1 g). The grounded powder was calcined at 500 °C for 4 h inside a programmable muffle furnace to convert to an oxidized form. Finally, the NPs were used for different characterizations. A 1.5 wt% dispersion of undoped and Mn-doped NiO NPs was prepared by dissolving 0.075 g of NPs in 5 mL of isopropyl alcohol (IPA) under vigorous sonication (Digital ultrasonic cleaner, LABTRON) at 40 kHz for 10 min. Then waited for few a minute to cool down the dispersal and spin-coated on pre-cleaned glass substrates at 3000 rpm for 30 s. Finally, the films were annealed on a hot plate for 15 min at 110 °C to remove IPA from the ~50 nm thin film.

Characterization

Undoped NiO and Mn-doped NiO NPs powers crystallographic evidence was characterized using X-ray Diffraction (XRD) (Cu Kα radiation, λ = 0.15406 nm, 40 kV and 60 mA, scanning range of 25°–90°, ARL Equinox 1000, Thermo Scientific™, USA), the surface morphology and elemental composition was explored using Field Emission Scanning Electron Microscopy (FE-SEM) (JEOL-7610F, Japan) equipped with Energy Dispersive Spectroscopy (EDS) (JEOL-JED2300 Analysis station, Japan), undoped NiO and Mn-doped NiO NPs thin film (NPsTF) prepared on glass substrate were used for contrasting compositional details with the chemical state using X-ray photoelectron spectroscopy (XPS, K-alpha, Thermo Scientific™, USA), and optical absorption was measured using UV-visible spectroscopy (UV-vis) (UH4150 Spectrophotometer (Integrating Sphere), Hitachi, Japan) from 280 nm to 800 nm at 600 nm per minutes scanning rate. The Hall effect measurement equipment (HMS ECOPIA 3000) was employed to determine the electrical parameters of all the samples, including resistivity, carrier concentration, and mobility, with a magnetic field of 0.57 T and a probe current of 40 nA.

SCAPS-1D simulation

The impact of Mn doped NiO NPs on the performances of the PSCs were examined using SCAPS-1D simulation software.[35,36] For the regeneration p–i–n junction with an inverted assembly was considered with the succeeding planar device structure: glass/ITO/NiO/MAPbI$_3$/PCBM/Al. The interface flanked by NiO/MAPbI$_3$ and MAPbI$_3$/PCBM was considered to have a neutral defect concentration of 1×10^{10} cm^{-2}.

Results and discussion

Structural analysis

Fig. 1 represents the XRD outline of the synthesized Mn-doped NiO (Mn = 0, 2, 4, 6, and 8 wt%) NPs. The occurrence of sharp diffraction peaks (2θ) to be found at 37.29°, 43.34°, 62.94°, 75.42°, and 79.46° corresponding to (111), (200), (220), (311), and (222) crystal planes respectively. The results indicated the face-centered cubic phase structure of NiO (JCPDS card no. 01-1239). The intensity of these reflections started decreasing with the increase of Mn doping percentage. In addition, all the reflections slightly shifted towards higher 2θ angles with the increase of Mn doping percentage. Increasing Mn doping likely introduces lattice distortions, defects, and disorder in the NiO structure, leading to reduced crystallinity. This decrease in crystallinity, along with potential smaller crystallite sizes, leads to a reduction in XRD peak intensity as well as slight shifting of the reflections.[16] The reflection positions shifting of the (200) plane is listed in Table 2. No additional reflection was observed due to Mn doping, even up to 8% doping, indicating Mn ions easily substituted Ni ions without affecting the crystal structure. The ionic radii of (Mn^{2+}), (Mn^{3+}), and (Mn^{4+}) are 0.83, 0.65, and 0.53 Å respectively, which is close or less than the ionic radii of (Ni^{2+}) 0.69 Å and (Ni^{3+}) 0.56 Å.[15]

The average crystallite size (D_{hkl}) was appraised by means of the Debye–Scherrer's equation:[40]

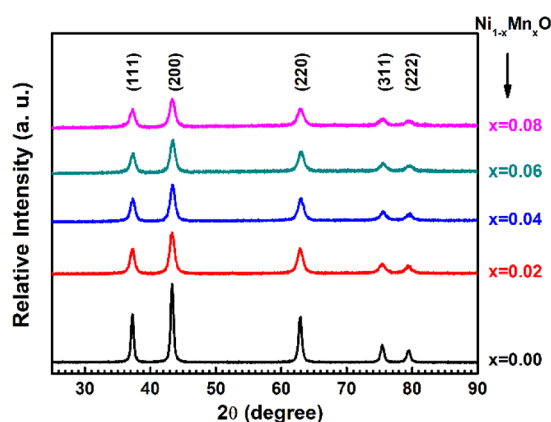$$D_{hkl} = \frac{k\lambda}{\beta \cos(2\theta)} \quad (1)$$

Fig. 1 XRD pattern analysis of pure NiO and Mn-doped NiO NPs.

Table 1 List of simulation parameter for perovskite based inverted solar cell[a]

Properties	PCBM (ETL)[37,38]	Perovskite (MAPbI$_3$)[39]	NiO (HTL)[27,28]				
			a	b	c	d	e
Thickness (nm)	70	320	50 (exp.)	50 (exp.)	50 (exp.)	50 (exp.)	50 (exp.)
Bandgap, E_g (eV)	2.1	1.56	3.49 (exp.)	3.69 (exp.)	3.74 (exp.)	3.79 (exp.)	3.91 (exp.)
Electron affinity, x_e (eV)	4.1	3.90	1.8	1.8	1.8	1.8	1.8
Dielectric permittivity, ϵ_r (relative)	4	10	11.75	11.75	11.75	11.75	11.75
CB effective density of states, N_C (cm^{-3})	2.5×10^{21}	2.76×10^{18}	2.0×10^{18}	2.0×10^{18}	2.0×10^{18}	2.0×10^{18}	2.0×10^{18}
VB effective density of states, N_V (cm^{-3})	2.5×10^{21}	3.90×10^{18}	2.0×10^{18}	2.0×10^{18}	2.0×10^{18}	2.0×10^{18}	2.0×10^{18}
Electron thermal velocity (cm s^{-1})	1×10^7	1×10^7	10^7	10^7	10^7	10^7	10^7
Hole thermal velocity (cm s^{-1})	1×10^7	1×10^7	10^7	10^7	10^7	10^7	10^7
Electron mobility (cm^2 V^{-1} s^{-1})	0.01	15	8	8	8	8	8
Hole mobility (cm^2 V^{-1} s^{-1})	0.01	15	211 (exp.)	249 (exp.)	469 (exp.)	1310 (exp.)	62.60 (exp.)
Shallow uniform acceptor density, N_A (cm^{-3})		1×10^{11}	6.32×10^{10} (exp.)	7.30×10^{10} (exp.)	1.16×10^{11} (exp.)	2.14×10^{11} (exp.)	3.89×10^{11} (exp.)
Shallow uniform donor density, N_D (cm^{-3})	5×10^{17}	1×10^{11}	—	—	—	—	—

[a] a – Pure NiO, b – 2, c – 4, d – 6, and e – 8 wt% Mn doped NiO HTL layer.

The wavelength of the X-ray, denoted by λ, is accompanied by the Full Width at Half Maxima (FWHM) intensity of the primary peak detected at 2θ in radian, referred to as β. Additionally, θ represents Bragg's angle of diffraction, while k signifies a constant. In addition the lattice parameter (a), dislocation density (δ), microstrain (ε), and stress (σ_s) of the NiO crystals were calculated using the following equations:[40]

$$a = d_{hkl} \times \sqrt{\left(h^2 + k^2 + l^2\right)} \tag{2}$$

$$\delta = \frac{1}{\left(D_{hkl}\right)^2} \tag{3}$$

$$\varepsilon = \frac{\beta}{4\tan\theta} \tag{4}$$

$$\sigma_s = \frac{Y(a - a_0)}{2a_0\gamma} \tag{5}$$

where, d_{hkl} is the inter planar spacing, hkl are miller indices, Y is the Young's modulus (220 GPa),[41] γ is the Poisson ration (0.3),[41] a is the samples' lattice constant calculated from the XRD data and a_0 is the lattice constant (4.1710 Å) obtained from JCPDS card no. 01-1239. The reflection position (2θ), FWHM (β), crystalline size (D_{hkl}), microstrain (ε), dislocation density (δ), and stress (σ_s) calculated using the (200) plane of NiO thin films is listed in Table 2. The FWHM value suddenly increased from 0.59 to 0.77 for pure NiO NPs to 2% Mn doped NiO NPs and then continuously increased to 0.78, 0.80, and 0.86 for 4, 6 and 8% Mn doping respectively. The calculated crystallite size was 15.26 nm for pure NiO NPs. In the case of Mn doped NiO NPs the crystallite size was reduced to 11.58, 11.45, 11.14, and 10.38 nm for 2, 4, 6, and 8% respectively. The dislocation density and microstrain of the pure NiO NPs was calculated to be 4.37×10^{-3} nm^{-2} and 6.48×10^{-3}% and increased with increasing Mn doping percentage to NiO. On the other hand, the stress of NiO NPs crystals did not show any trend. Mn interacts differently with oxygen compared to Ni due to its ability to form various oxidation states, influencing the crystal structure of materials. Mn can exhibit multiple oxidation states, leading to the formation of diverse crystal structures with oxygen, impacting the material's properties.[16] In contrast, nickel typically forms stable compounds with oxygen, resulting in a more limited range of crystal structures compared to manganese.[42] The interaction between Mn and O can introduce structural distortions and changes in the lattice parameters, affecting the overall stability, optical and electronic properties of the material.[43] Therefore, the distinct behavior of Mn in interacting with oxygen compared to Ni plays a crucial role in determining the crystal structure and properties of materials in various applications.

Surface morphology and particle size analysis

Fig. 2 shows the FE-SEM morphological images of Ni$_{1-x}$Mn$_x$O NPs ($x = 0.00, 0.02, 0.04, 0.06,$ and 0.08). NiO NPs (Fig. 2(a)) are homogeneous with limited size distribution. However, the shape of the nanoparticles became smaller in size forming

Table 2 Extracted physical properties of synthesized $Ni_{1-x}Mn_xO$ NPs using the (200) plane of Fig. 1

Sample $Ni_{1-x}Mn_xO$ ($x =$)	Structural properties derived from (200) plane						
	2θ (degree)	β (degree)	a (Å)	D_{200} (nm)	$\varepsilon \times 10^{-3}$ (%)	$\delta \times 10^{-3}$ (nm^{-2})	σ_s (GPa)
0.00	43.32	0.59	4.17	15.26	6.48	4.37	0.40
0.02	43.33	0.77	4.17	11.58	8.46	7.44	0.45
0.04	43.39	0.78	4.17	11.45	8.55	7.63	−0.07
0.06	43.41	0.80	4.17	11.14	8.79	8.06	−0.19
0.08	43.36	0.86	4.17	10.38	9.44	9.28	0.26
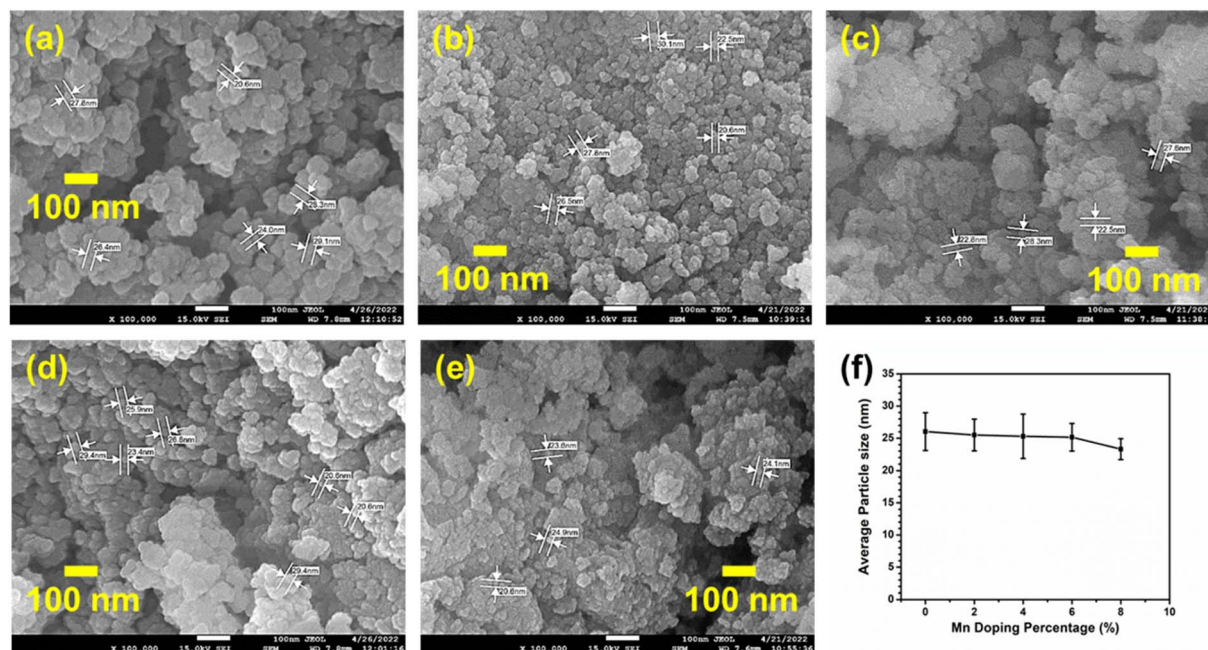
Fig. 2 FE-SEM morphological images of the synthesized $Ni_{1-x}Mn_xO$ NPs: $x =$ (a) 0, (b) 0.02, (c) 0.04, (d) 0.06, (e) 0.08 and variation of average particle size of NiO NPs with Mn doping percentage (f).

spherical multicore-like structures[17,44] following doping (Fig. 2(b)–(e)). The incorporation of Mn ions to the NiO lattice during the nucleation and growth alters the size and morphology of $Ni_{1-x}Mn_xO$ NPs.[45] These alterations in crystal shape and size are crucial in understanding the impact of Mn doping on the structural properties of NiO, which is significant for various technological applications such as photocatalysis and energy storage devices. Fig. 2(f) shows the average grain size variation against Mn doping percentage of $Ni_{1-x}Mn_xO$ NPs, measured by FE-SEM. The average particle size observed to be 26.03, 25.50, 25.30, 25.15, and 23.3 nm for 0, 2, 4, 6, and 8% Mn-doped NiO NPs respectively. As the Mn doping increases in NiO NPs the strain of the crystals dominates to decrease the size of NPs.[46] Which is understandable with the evidence of the XRD data.

EDS measurements demonstrate that the generated NPs had Ni and O peaks, which is compatible with the XRD results. The EDS spectrum of Mn-doped NiO nanoparticles (Mn = 0, 2, 4, 6, and 8 wt%) is shown in Fig. 3(a)–(e) shows just Ni, O, and Mn peaks (neglecting the peaks for platinum, as it was coated during the FE-SEM measurement process to form conductive layer), indicating the samples' high purity.

The elemental composition of Mn-doped NiO (Mn = 0, 2, 4, 6, and 8 wt%) nanoparticles are given in Table 3 which was found from EDS spectrum analysis.

In pure NiO, the stoichiometric atomic percentages of Ni and O are 77.48% and 22.52% by weight, respectively. In all the samples, the oxygen weight percentage is lower, and the Ni to O and Mn to O demonstrates the non-stoichiometric nature of NiO. The NiO ratio deviates from 1 : 1, indicating non-stoichiometry. This non-stoichiometry leads to a color shift in NiO, with stoichiometric NiO appearing green and non-stoichiometric NiO appearing black. Nickel acetate tetrahydrate $[C_4H_6NiO_4 \cdot 4H_2O]$ was employed as a precursor in the synthesis of NiO NPs. Before synthesis, it was green, but after the production of NiO NPs, it turned black, clearly demonstrating the non-stoichiometric nature of NiO and the increased presence of oxygen vacancies. The presence of Mn atomic
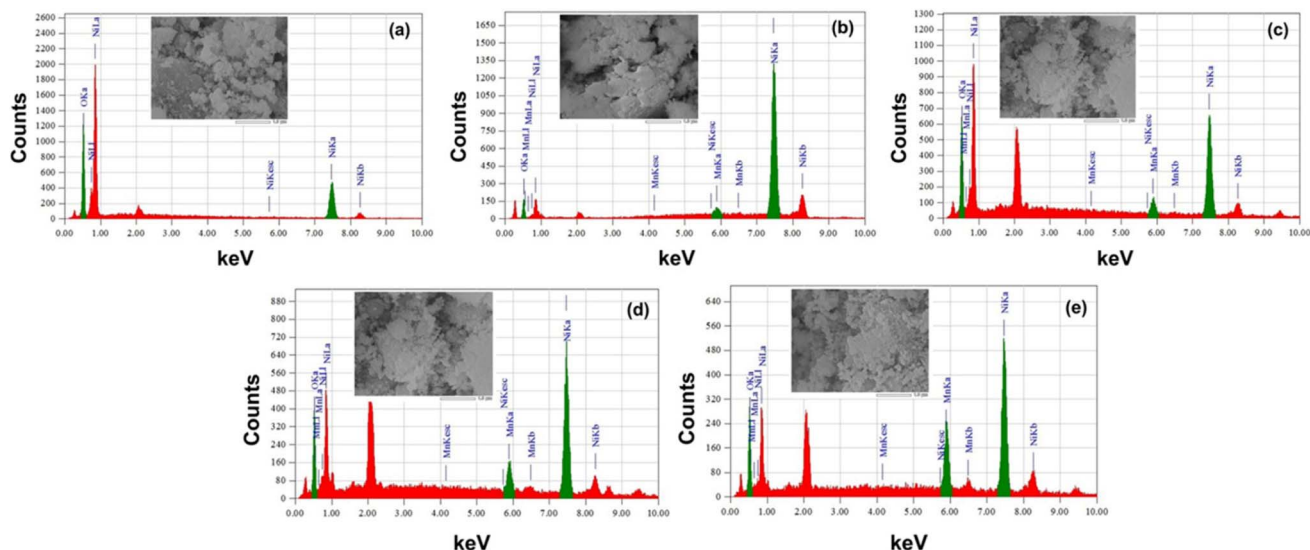
Fig. 3 EDS spectrum of the synthesized $Ni_{1-x}Mn_xO$ NPs: (a) $x = 0$, (b) $x = 0.02$, (c) $x = 0.04$, (d) $x = 0.06$, (e) $x = 0.08$.

Table 3 Elemental composition of pure NiO and Mn doped NiO NPs characterized by EDS analysis

Sample	Atomic percentage (%)		
	Ni	O	Mn
Pure NiO	77.48	22.52	0.00
2% Mn doped NiO	82.95	15.23	1.82
4% Mn doped NiO	79.30	17.05	3.65
6% Mn doped NiO	77.11	18.23	4.66
8% Mn doped NiO	74.10	18.85	7.05

percent in the doped samples indicate Mn was successfully doped into the NiO lattice.

The surface elemental composition and valence state analysis

The XPS exploration provided important insights into the chemical composition and oxidation states of the nanoparticles, highlighting the impact of Mn doping on the oxidation state of nickel within the NiO structure. The binding energies were determined using the C 1s peak as a reference point (284.5 eV). Following that, all the obtained data underwent a careful deconvolution procedure, which was skillfully performed using the XPSPEAK41 simulation program. Black lines visually indicate raw data, whereas dotted red lines signify simulated data. Furthermore, the deconvoluted peaks, which were expertly suited to the simulated data, are shown by lines of varying hues.

The deconvoluted Ni 2p XPS spectra of pure NiO NPs revealed (Fig. 4(a) bottom side) distinguishing $2p_{3/2}$ spin–orbit peaks at the binding energy of 853.8, 855.8, and 862 eV, $2p_{1/2}$ spin–orbit peaks at the binding energy of 871.5, 873.5, and 880 eV for Ni^{2+}, Ni^{3+}, and corresponding satellite peaks respectively. The O 1s XPS spectra of undoped NiO NPs show (Fig. 4(b) bottom side) a prominent peak at 529.6 eV, corresponding to NiO and relatively lower intensity peak at 531.7 eV for Ni_2O_3.[47,48] No other additional peak was observed.

In the case of the 6 wt% Mn-doped NiO NPs sample, the deconvoluted Ni 2p XPS spectra similarly showed (Fig. 4(a) top side) distinguishing $2p_{3/2}$ spin–orbit peaks at the binding energy of 853.9, 855.9, and 861.7 eV, $2p_{1/2}$ spin–orbit peaks at the binding energy of 872.1, 873.7, and 880 eV for Ni^{2+}, Ni^{3+}, and conforming satellite peaks in that order. On the other hand, the O 1s XPS spectra show (Fig. 4(b) top side) relatively low intensity peak at 529.6 eV for NiO, a prominent peak at 531.7 eV, corresponding to Ni_2O_3 and an additional peak at 529.8 eV for MnO_2. The deconvoluted Mn 2p XPS spectra depicted (Fig. 4(c)) characteristic $2p_{3/2}$ spin–orbit peak at the binding energy of 641.6 eV and $2p_{1/2}$ spin–orbit peak at the binding energy of 652.9 eV for MnO_2.[47,48]

The XPS results confirmed that synthesized pure NiO with preferred oxidation state of Ni^{2+} but 6 wt% Mn-doped NiO NPs e preferred oxidation state of Ni^{3+}. This higher oxidation state of Ni^{3+} in the Mn doped nanoparticles could be attributed to the influence of the Mn dopant on the electronic structure of the NiO matrix, leading to changes in the oxidation states of the nickel ions.[49] In the case of 6 wt% Mn-doped NiO NPs, Mn ions oxidation state is Mn^{4+}. This result helps understand the structural and morphological data.

Optical properties analysis

The optical absorption spectra of $Ni_{1-x}Mn_xO$ ($x = 0.0, 0.02, 0.04, 0.06$, and 0.08) NPs thin films were measured using a UV-vis spectrophotometer in the region of 300 to 800 nm which is shown in Fig. 5(a). The absorption edge shifting towards lower wavelength was observed (Fig. 5(b)) due to the shrinkage in crystallite size with incorporating dopant concentration of Mn, indicating a blue shift.[50]

The optical bandgap, E_g, of Mn-doped NiO (Mn = 0, 2, 4, 6, and 8 wt%) NPs thin film was calculated using the Tauc plot.
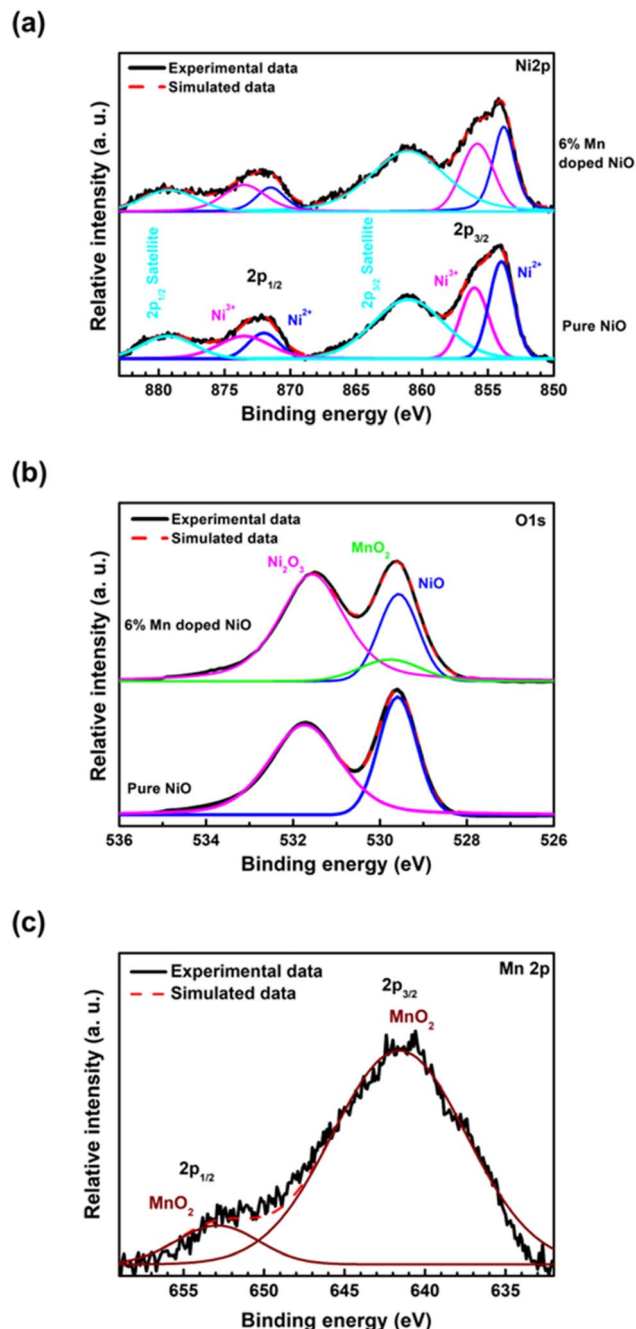
Fig. 4   The XPS spectra of (a) Ni 2p, (b) O 1s (bottom side pure NiO and top side 6% Mn-doped NiO NPs), NiO, and (c) Mn 2p of 6% Mn-doped NiO NPs.

The direct band gap values for the samples are obtained by the Tauc method as follows:

$$(\alpha h\nu)^n = A(h\nu - E_g) \qquad (6)$$

In eqn (6), α is the absorption coefficient of the NPs, A is a constant, E_g is the energy bandgap, $h\nu$ is the incident photon energy and n is an index and can have values i.e. 2, 3, 1/2, 1/3 which depends on the band-to-band transition. During the
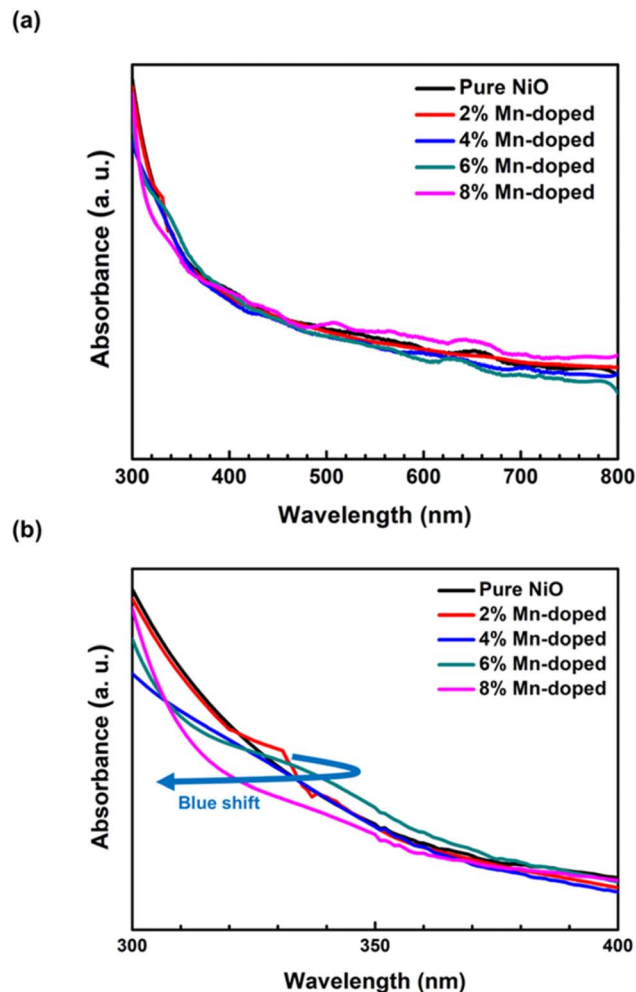

Fig. 5   Optical absorption spectra of the NiO and Mn-doped NiO thin films (a) full visible range, and (b) enlarged within 300 to 400 nm wavelengths.

band gap computation, it is observed that for $n = 2$, eqn (6) provides the best linear fit on the projection of the Tauc plot as shown in Fig. 6(a)–(e). The plots are drawn as $\alpha h\nu^2$ versus $h\nu$. The straight linear portion of this curve is extrapolated onto the horizontal axes, and energy band gap values are achieved for different Mn/NiO ratios.

The values of the bandgap of undoped NiO, 2, 4, 6, and 8 wt% Mn-doped NiO NPs were confirmed to be 3.49, 3.69, 3.74, 3.79, and 4.10 eV respectively, as depicted in Fig. 6(a)–(e). Fig. 6(f) shows the synthesized NiO NPs' optical bandgap variation against the Mn doping concentration. The optical bandgap values increase with Mn doping. Mn incorporation into NiO NPs decreases the average crystallite size, indicating a size-reduction effect.[17,51,52] Additionally, the optical band gap of the Mn-doped NiO NPs increases due to the quantum size effect, with a shift towards higher energy levels observed in the UV-vis absorption spectra.[17,51,52] These changes in size and band gap are crucial for tuning the properties of the nanoparticles, making them potentially useful in applications such as photocatalysis and magnetic materials with tailored optical characteristics.
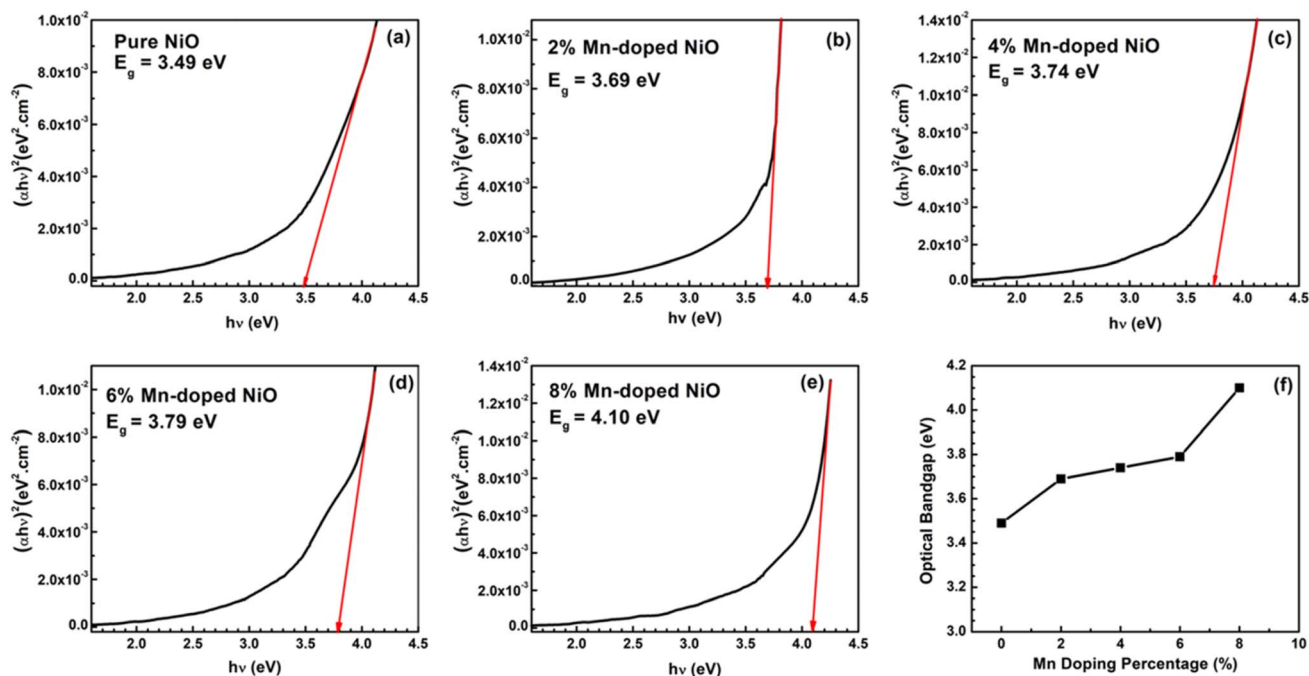
Fig. 6 Tauc plot of the $Ni_{1-x}Mn_xO$ NPs: (a) $x = 0$, (b) $x = 0.02$, (c) $x = 0.04$, (d) $x = 0.06$, (e) $x = 0.08$. And variation of NiO NPs optical bandgap with different Mn doping concentrations (f).

Electrical properties analysis

The Hall Effect was determined of pure NiO and Mn-doped NiO NPs thin film (TF) samples using the van der Pauw method[53] and illustrated in Fig. 7. All the samples revealed p-type features, signifying that the material had more holes than electrons. The pure NiO thin film showed bulk concentration, carrier mobility, and resistivity of $6.32 \pm 0.63 \times 10^{10}$ cm^{-3}, $2.11 \pm 0.28 \times 10^2$ cm^2 V^{-1} s^{-1}, and $3.97 \pm 0.21 \times 10^5$ Ω.cm in that order. The bulk concentration increased with increasing Mn doping percentage (Fig. 7(a)), $7.30 \pm 0.59 \times 10^{10}$, $1.16 \pm 0.10 \times 10^{11}$, $2.14 \pm 0.09 \times 10^{11}$, and $3.89 \pm 0.14 \times 10^{11}$ cm^{-3} for 2, 4, 6, and 8 wt% doping of Mn respectively (Fig. 7(a)). Mn doping in NiO nanoparticles results in a significant increase in bulk charge carrier concentration, as indicated by Hall measurements. This phenomenon can be attributed to the substitution of Ni^{2+} and Ni^{3+} ions by Mn^{4+} ions or the insertion of Mn^{4+} ions into vacant interstitial sites within the NiO lattice. Both the case generates access holes in the lattice system leading to bulk carrier concentration increase.

The mobility of charge carriers in NiO nanoparticles doped with varying concentrations of Mn (2, 4, 6, and 8 wt%) reveals a distinguished tendency: an initial increase, hit the highest point at 6 wt%, followed by a decrease at 8 wt% (Fig. 7(b)). This behavior can be explained by considering the impact of Mn doping on the NiO lattice structure and the resulting charge carrier dynamics.

The trend in mobility with increasing Mn doping reflects a balance between enhancing carrier concentration and minimizing structural defects and scattering centers. The resistivity of NiO nanoparticles doped with varying concentrations of Mn (2, 4, 6, and 8 wt%) shows (Fig. 7(c)) a trend opposite to that of mobility: it decreases initially, reaching a minimum at 6 wt%, and then increases at 8 wt%. This behavior can be explained by examining the interplay between carrier concentration and mobility, as resistivity is inversely proportional to the bulk concentration and mobility. The observed trends in resistivity and mobility with varying Mn doping levels reflect the delicate balance between carrier concentration and mobility. The increase in resistivity at higher doping levels (8 wt%) is primarily due to the significant reduction in mobility, which dominates over the effect of the high carrier concentration.

Numerical simulation

SCAPS 1D software was utilized to numerically model inverted PSCs using the electrical characteristics obtained from electrical property study of pure and Mn-doped NiO TFs.

The electrical parameters of various layers employed during the simulation are reported in Table 1. Fig. 8(a) depicts the current density V_s applied voltage curve for the devices with various Mn-doped NiO HTL layers. All the devices had identical short circuit current (J_{SC}) and open circuit voltage (V_{OC}) but due to their efficiency (η) differed based on their fill factor (FF) (Fig. 8(b)). The device with pure NiO HTL layer had the η of 14.66%. Devices using 2, 4, 6, and 8 wt% Mn-doped NiO HTL layers exhibited η of 15.68, 16.35, 17.07, and 13.71% in that order. 6 wt% Mn-doped NiO thin film showed the highest mobility with the lowest resistivity, leading to best performance device.
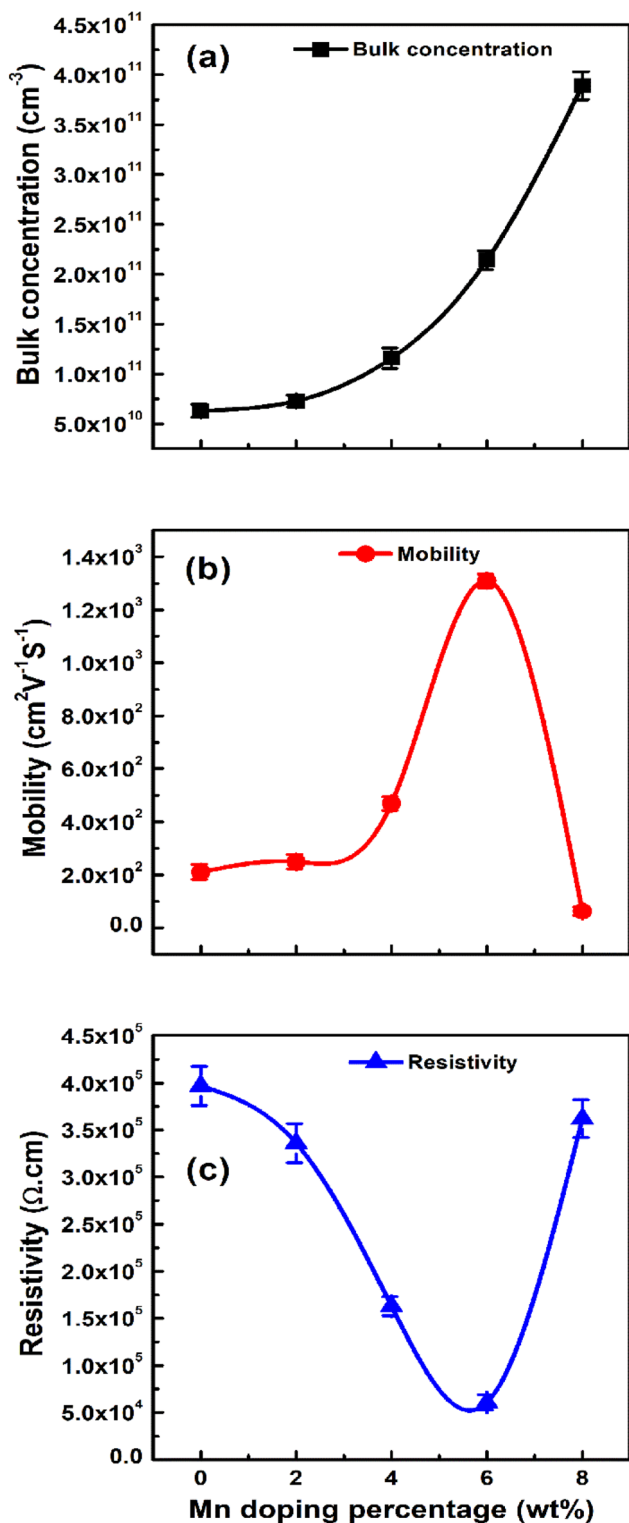
Paper

Fig. 7 (a) Bulk concentration variation of the bulk NiO NPs thin films, (b) mobility of free carriers in the NiO NPs thin films, and (c) resistivity of the NiO NPs thin films variation with Mn doping percentage.
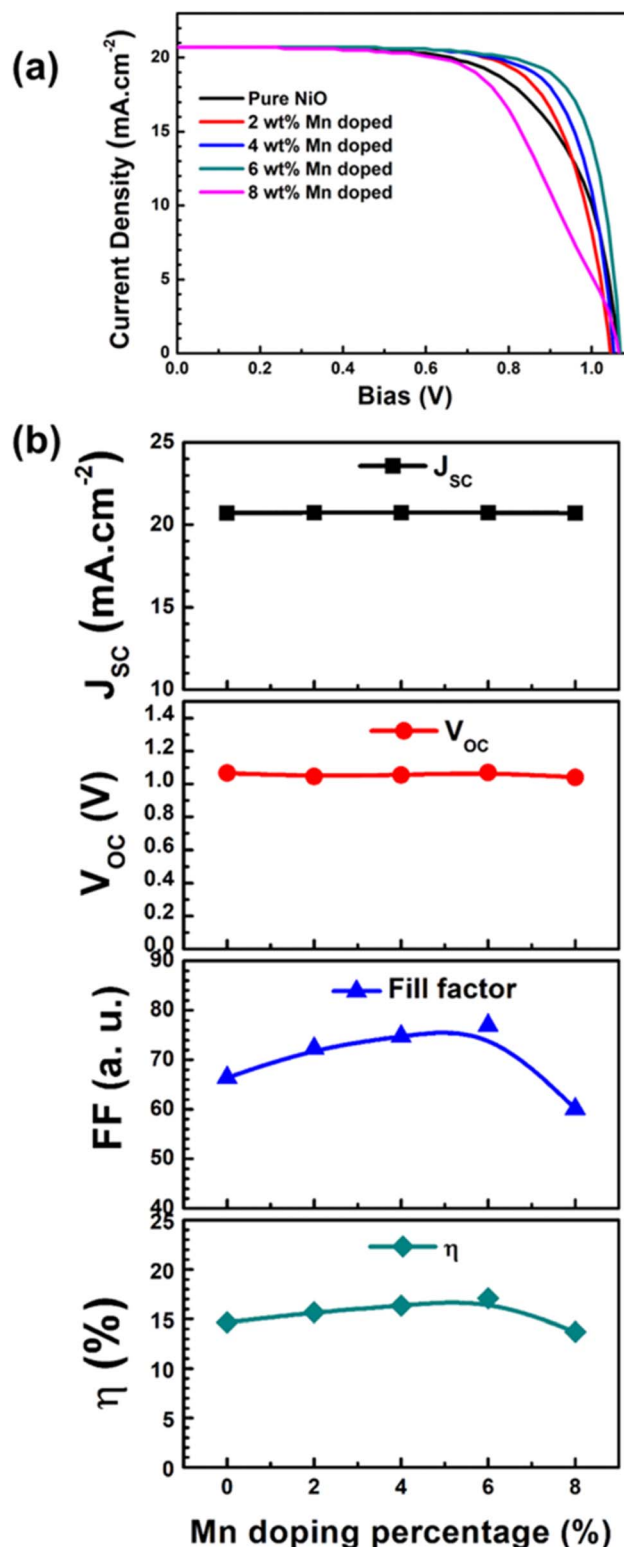

Fig. 8 (a) J–V curve of SCAPS-1D simulated Perovskite based solar cells using synthesized pure and Mn-doped NiO NPs thin film based HTL layer and (b) device performance parameter variation of different devices.

Conclusion

This study successfully synthesized highly crystalline face-centered cubic (FCC) nanoparticles (NPs) of pure and Mn-doped NiO through a chemical precipitation process, achieving uniform size distribution. The average particle size decreased from 26.03 nm to 23.30 nm with the increasing Mn

doping concentration. This reduction in size induced quantum confinement phenomena leading to a blue shift in the optical absorbance. Importantly, the optical bandgap expansion from 3.49 (pure NiO) to 4.10 (8 wt% Mn-doped NiO) eV highlights the tunability of optical properties *via* controlled doping. The X-ray Photoelectron Spectroscopy (XPS) revealed shifts in oxidation states with Mn doping, indicating the presence of Ni^{3+} and Mn^{4+}, which significantly influence the electronic structure of the NPs.

The enhancement in carrier mobility, peaking at 6 wt% Mn doping, further underscores the potential of Mn-doped NiO for electronic applications, as confirmed by Hall measurements. SCAPS-1D simulations demonstrated the efficacy of the synthesized NPs in perovskite solar cells (PSCs), achieving a peak power conversion efficiency (PCE) of 17.07% with 6 wt% Mn-doped NiO NPs as the hole transport layer (HTL). These findings pave the way for further exploration of Mn-doped NiO in photovoltaic devices, offering a viable route toward the development of high-efficiency, stable solar cell technologies. Future research may explore optimizing doping concentrations and exploring other transition metals to further enhance the performance of such devices.

Data availability

The authors confirm that the data supporting the findings of this study are available within the article.

Author contributions

R. I.: data curation, formal analysis, investigation, validation, writing – original draft. R. A.: data curation, formal analysis, investigation, methodology, visualization, validation, supervision, writing – review & editing. M. A. A.: investigation, validation. N. M.: data curation, validation. A. N. A.: data curation, validation. M. S. B.: data curation, validation. D. I.: data curation, validation. M. H.: supervision, writing – review & editing, funding acquisition. M. S. J.: conceptualization, funding acquisition, project administration, validation, supervision, writing – review &editing.

Conflicts of interest

The authors declare that they have no conflict of interest.

Acknowledgements

References

1 A. Verma and B. C. Yadav, in *Complex and Composite Metal Oxides for Gas, VOC and Humidity Sensors*, Elsevier, 2024, vol. 2, pp. 3–25.

2 H. Kaur and S. S. Siwal, in *Metal Oxides for Next-Generation Optoelectronic, Photonic, and Photovoltaic Applications*, Elsevier, 2024, pp. 253–276.

3 U. Chakraborty, B. Sharma, G. Kaur and G. R. Chaudhary, *Metal Oxide Nanostructure for Biomedical Application*, Springer, Singapore, 2024, pp. 43–69.

4 L. Calió, S. Kazim, M. Grätzel and S. Ahmad, *Angew. Chem., Int. Ed.*, 2016, **55**, 14522–14545.

5 L. G. Teoh and K.-D. Li, *Mater. Trans.*, 2012, **53**, 2135–2140.

6 Q. Li, L.-S. Wang, B.-Y. Hu, C. Yang, L. Zhou and L. Zhang, *Mater. Lett.*, 2007, **61**, 1615–1618.

7 X. Xin, Z. Lü, B. Zhou, X. Huang, R. Zhu, X. Sha, Y. Zhang and W. Su, *J. Alloys Compd.*, 2007, **427**, 251–255.

8 J. H. Kim, P.-W. Liang, S. T. Williams, N. Cho, C.-C. Chueh, M. S. Glaz, D. S. Ginger and A. K.-Y. Jen, *Adv. Mater.*, 2015, **27**, 695–701.

9 Y. J. Mai, J. P. Tu, X. H. Xia, C. D. Gu and X. L. Wang, *J. Power Sources*, 2011, **196**, 6388–6393.

10 S. Ghazal, N. Khandannasab, H. A. Hosseini, Z. Sabouri, A. Rangrazi and M. Darroudi, *Ceram. Int.*, 2021, **47**, 27165–27176.

11 N. A. Mala, S. Sivakumar, K. M. Batoo and M. Hadi, *Inorg. Chem. Commun.*, 2021, **131**, 108797.

12 S. Sivakumar and N. Ahmad Mala, *Mater. Today: Proc.*, 2022, **49**, 1469–1474.

13 Z. Xiao, W. Zhou, N. Zhang, C. Liao, S. Huang, G. Chen, G. Chen, M. Liu, X. Liu and R. Ma, *Chem. Commun.*, 2021, **57**, 6070–6073.

14 J. Chen, X. Peng, L. Song, L. Zhang, X. Liu and J. Luo, *R. Soc. Open Sci.*, 2018, **5**, 180842.

15 W. Yan, Z. Sun, Z. Li, Q. Liu, T. Yao, Z. Pan, C. Wang, F. Hu, Y. Jiang, Z. Qi, F. Zeng and S. Wei, *Adv. Mater.*, 2012, **24**, 353–357.

16 N. R. Aswathy, J. Varghese, S. R. Nair and R. V. Kumar, *Mater. Chem. Phys.*, 2022, **282**, 125916.

17 C. Thangamani, P. Vijaya Kumar, K. Gurushankar and K. Pushpanathan, *J. Mater. Sci. Mater. Electron.*, 2020, **31**, 11101–11112.

18 X. Jiang, C. Li, Y. Gao, C. Yang, F. You and C. Yao, *Nano*, 2018, **13**, 1850017.

19 V. Ganesh, B. R. Kumar, Y. Bitla, I. S. Yahia and S. AlFaify, *J. Inorg. Organomet. Polym. Mater.*, 2021, **31**, 2691–2699.

20 S. Layek and H. C. Verma, *J. Magn. Magn. Mater.*, 2016, **397**, 73–78.

21 P. Nivedha, S. Monika and S. Devikala, *Mater. Today: Proc.*, 2022, **50**, 380–383.

22 M. Jamal, S. A. Shahahmadi, P. Chelvanathan, H. F. Alharbi, M. R. Karim, M. Ahmad Dar, M. Luqman, N. H. Alharthi, Y. S. Al-Harthi, M. Aminuzzaman, N. Asim, K. Sopian, S. K. Tiong, N. Amin and M. Akhtaruzzaman, *Results Phys.*, 2019, **14**, 102360.

23 M. S. Jamal, M. S. Chowdhury, S. Bajgai, M. Hossain, A. Laref, P. K. Jha and K. Techato, *Mater. Res. Express*, 2021, **8**, 126404.

24 A. K. Mahmud Hasan, M. S. Jamal, N. Kamaruddin, N. Asim, K. Sopian, M. Akhtaruzzaman and O. Raed, in *2019 6th*

International Conference on Space Science and Communication (IconSpace), IEEE, 2019, pp. 267–270.

25 M. B. Islam, M. Yanagida, Y. Shirai, Y. Nabetani and K. Miyano, *ACS Omega*, 2017, **2**, 2291–2299.

26 M. S. Jamal, K. Sobayel, H. Misran, T. Nasrin, K. Althubeiti, H. I. Alkhammash, M. Shahiduzzaman, K. Sopian, N. Amin and M. Akhtaruzzaman, *Appl. Sci.*, 2021, **11**, 11546.

27 H. Steinebach, S. Kannan, L. Rieth and F. Solzbacher, *Sensor. Actuator. B Chem.*, 2010, **151**, 162–168.

28 M. R. Hasan, T. Xie, S. C. Barron, G. Liu, N. V. Nguyen, A. Motayed, M. V. Rao and R. Debnath, *APL Mater.*, 2015, **3**, 106101.

29 S. Pereira, A. Gonçalves, N. Correia, J. Pinto, L. Pereira, R. Martins and E. Fortunato, *Sol. Energy Mater. Sol. Cells*, 2014, **120**, 109–115.

30 A. Kumar, M. A. Mustafa, A. Fouly, P. S. Bains, R. Sharma, Y. S. Bisht, E. M. Awwad and P. Singh, *RSC Adv.*, 2024, **14**, 13374–13383.

31 Z. Golshani, F. Arjmand, S. Maghsoudi and S. M. A. Hosseini, *J. Mater. Res. Technol.*, 2023, **23**, 2612–2625.

32 A. Intaniwet, P. Makming, S. Homnan, P. Ruankham, D. Wongratanaphisan, Y. Chimupala, F. Goubard and A. Adjaoud, *Suan Sunandha Sci. Technol. J.*, 2022, **9**, 71–78.

33 H. Wang, Z. Qin, X. Li, C. Zhao and C. Liang, *Energy Environ. Mater.*, 2024, **7**(4), e12666.

34 X. Cai, T. Hu, H. Hou, P. Zhu, R. Liu, J. Peng, W. Luo and H. Yu, *Mater. Today Sustain.*, 2023, **23**, 100438.

35 M. Burgelman, P. Nollet and S. Degrave, *Thin Solid Films*, 2000, **361–362**, 527–532.

36 M. S. Chowdhury, S. A. Shahahmadi, P. Chelvanathan, S. K. Tiong, N. Amin, K. Techato, N. Nuthammachot, T. Chowdhury and M. Suklueng, *Results Phys.*, 2020, **16**, 102839.

37 L. Moulaoui, O. Bajjou, A. Najim, M. Archi and K. Rahmani, in *2022 2nd International Conference on Innovative Research in Applied Science, Engineering and Technology (IRASET)*, IEEE, 2022, pp. 1–7.

38 U. Mandadapu, *Indian J. Sci. Technol.*, 2017, **10**, 1–8.

39 M. S. Rahman, S. Miah, M. S. W. Marma and T. Sabrina, in *2019 International Conference on Electrical, Computer and Communication Engineering (ECCE)*, IEEE, 2019, pp. 1–6.

40 Z. Aba, A. Goktas and A. Kilic, *J. Sol-Gel Sci. Technol.*, 2024, **109**, 260–271.

41 M. Pihlatie, A. Kaiser and M. Mogensen, *J. Eur. Ceram. Soc.*, 2009, **29**, 1657–1664.

42 S. M. Kumawat, G. D. Dwivedi, T. W. Yen, D. C. Kakarla, A. Tiwari, S. M. Huang, S. J. Sun, H. D. Yang and H. Chou, *J. Alloys Compd.*, 2022, **919**, 165777.

43 M. Dinesh, Y. Haldorai and R. T. Rajendra Kumar, *Ceram. Int.*, 2020, **46**, 28006–28012.

44 İ. Adanur, T. Karazehir, B. Doğru Mert, M. Akyol and A. Ekicibil, *J. Chem. Phys.*, 2022, **156**(6), 064705.

45 D. Hong, W. Yan, Q. Liu, T. Yao, Z. Sun and S. Wei, *J. Phys. D Appl. Phys.*, 2014, **47**, 295001.

46 A. Das, A. C. Mandal, S. Roy and P. M. G. Nambissan, *J. Nanosci. Nanotechnol.*, 2016, **16**, 4153–4163.

47 Q. Hu, W. Li, D. I. Abouelamaiem, C. Xu, H. Jiang, W. Han and G. He, *RSC Adv.*, 2019, **9**, 20963–20967.

48 M. M. Rahman, M. M. Alam and A. M. Asiri, *RSC Adv.*, 2019, **9**, 35146–35157.

49 J. Pati, S. Priyadarshinee, R. Mahapatra, D. K. Mishra, J. Mohapatra and P. Mohanty, *Mater. Today: Proc.*, 2022, **67**, 1080–1084.

50 S.-J. Hong, H.-J. Mun, B.-J. Kim and Y.-S. Kim, *Micromachines*, 2021, **12**, 1168.

51 M. B. Shelar, K. M. Patil, S. K. Nalugade, V. R. Chavan, R. M. Jadhav, M. S. Kore and A. V. Gaikwad, *Mater. Sci. Res. India*, 2024, **21**, 11–17.

52 M. Jothibas, K. Bharanidharan, E. Paulson, M. Elayaraja, B. A. Kumar and A. Muthuvel, *J. Mater. Sci. Mater. Electron.*, 2022, **33**, 907–919.

53 F. S. Oliveira, R. B. Cipriano, F. T. da Silva, E. C. Romão and C. A. M. dos Santos, *Sci. Rep.*, 2020, **10**, 16379.